

Optimal design of unimorph-type cantilevered piezoelectric energy harvesters using level set-based topology optimization by considering manufacturability

Ken Miyajima^{a,b}, Takayuki Yamada^{b,c}

^a*Osaka Research Institute of Industrial Science and Technology, Ayumino-2-7-1, Izumi-city, 594-1157, Osaka, Japan*

^b*Department of Mechanical Engineering, Graduate School of Engineering, The University of Tokyo, Yayoi 2-11-16, Bunkyo-ku, 113-8656, Tokyo, Japan*

^c*Department of Strategic Studies, Institute of Engineering Innovation, Graduate School of Engineering, The University of Tokyo, Yayoi 2-11-16, Bunkyo-ku, 113-8656, Tokyo, Japan*

Abstract

In this study, we proposed a design methodology for a piezoelectric energy-harvesting device optimized for maximal power generation at a designated frequency using topology optimization. The proposed methodology emphasizes the design of a unimorph-type piezoelectric energy harvester, wherein a piezoelectric film is affixed to a singular side of a silicon cantilever beam. Both the substrate and the piezoelectric film components underwent concurrent optimization. Constraints were imposed to ensure that the resultant design is amenable to microfabrication, with specific emphasis on the etchability of piezoelectric energy harvesters. Several numerical examples were provided to validate the efficacy of the proposed method. The results showed that the proposed method derives both the substrate and piezoelectric designs that maximize the electromechanical coupling coefficient and allows the eigenfrequency of the device and minimum output voltage to be set to the desired values. Furthermore, the proposed method can provide solutions that satisfy the cross-sectional shape, substrate-depend, and minimum output voltage constraints. The solutions obtained by the proposed method are manufacturable in the field of microfabrication.

Keywords: Topology optimization, Piezoelectric material, Energy harvester, Manufacturability, Level set method

1. Introduction

Piezoelectric energy harvesters convert mechanical energy into electrical energy through the piezoelectric effect. These devices have gained significant attention in recent years owing to their potential to scavenge energy from various sources such as vibrations [1, 2] and fluid flow [3]. The design of a piezoelectric energy harvester plays a critical role in determining its efficiency and performance [4]. Various piezoelectric energy harvester designs, including cantilever beams, multilayered structures, and cylinder structures, have been proposed and studied [5, 6]. The unimorph cantilevered piezoelectric energy harvester has several advantages over the other piezoelectric energy harvester designs. The simple and compact design of this harvester makes it suitable for applications where size and weight are critical factors, such as in portable or wearable devices. Furthermore, the unimorph cantilevered design allows easy integration with other systems such as sensors or wireless transmitters [7]. However, the performance of a unimorph cantilevered piezoelectric energy harvester is limited by the amount of mechanical energy harvested from external vibrations. To overcome these limitations, researchers have explored the use of advanced materials and optimization techniques to improve the performance of unimorph cantilevered piezoelectric energy harvesters. Some studies have investigated piezoelectric materials with improved electromechanical coupling factors to enhance the piezoelectric effect and improve energy conversion efficiency [8, 9]. Other researchers have focused on designing the geometry of the cantilever beam and piezoelectric element for maximum energy output. For instance, rectangular, triangular, and trapezoidal shapes have been proposed for unimorph piezoelectric vibration energy harvesters [10]. However, as these structures have simple geometries, significant improvements can be achieved using topological optimization techniques [11].

Among the early forays in the topology optimization of piezoelectric materials, the study by Silva et al. [12] stood out as a pioneering study. This study explored the optimal design of periodic piezocomposites and underscored the profound impact of the unit cell topology on the performance of piezoelectric materials. Their insights provided a foundational framework for subsequent advancements in the field. The optimization of a piezoelectric energy harvester requires meticulous attention to numerous parameters, including the geometry and material properties of the piezoelectric element, resonant frequency of the device, and electrical load impedance. Zeng et

al. [13] introduced a topology optimization technique to maximize the harvesting performance of piezoelectric energy harvesters. Rupp et al. [14] conceived a design for a piezoelectric energy harvester integrated with an external electrical circuit with due regard to the electrical load impedance. Kögl et al. [15] advanced the “PEAMAP-P” analysis model, specifically tailored for the analytical modeling of piezoelectric materials. Their design paradigm singularly targeted the piezoelectric material domain and deliberately omitted the substrate domain. Conversely, Kang et al. [16] considered both the piezoelectric material and electrode domains in their design. Zhang et al. Adding a unique perspective, [17] focused on the dynamic responses in piezoelectric structures, emphasizing transient load optimization. Their approach highlights the need for a nuanced design in active-control smart structures. Chen et al. [18] and Luo et al. [19] designed tubular energy harvesting devices incorporating multiple materials. Notably, they employed level set-based topology optimization to eliminate grayscale discrepancies between the material and void domains. He et al. [20] and Almeida et al. [21] focused on designing the thickness profile of a piezoelectric energy harvester by considering the piezoelectric material, substrate, and electrode domains. In addition, Kim et al. [22] optimized both the substrate and piezoelectric material domains. They delineated distinct objective functions for each domain and sequentially optimized the substrate and piezoelectric film structures. Similarly, in the field of acoustic energy focusing, Yoon et al. [23] demonstrated the application of topology optimization for piezoelectric acoustic focusers. By considering the intricate interactions among the electric, mechanical, and acoustic phenomena, their approach offers a more comprehensive understanding and optimization of piezoelectric devices in acoustically challenging environments. In a notable advancement, Salas et al. [24] extended topology optimization in piezoelectric actuators beyond traditional metal substrates and piezoelectric films to include the optimization of fibers and polarization in laminated piezocomposite multi-entry actuators (LAPAs). This holistic approach presents a significant challenge in the design of sophisticated actuators with enhanced performance capabilities. To further develop their methods, Salas et al. [25] introduced the hybrid interpolation model for fiber orientation (HYIMFO) method, which harmonizes continuous and discrete fiber orientation optimization for the LAPA. This hybrid approach represents a progressive stride in the optimization of complex multi-material actuators. However, these methodologies often yield designs that face inherent manufacturing challenges. Consequently, various strate-

gies have been proposed to realize manufacturable designs through topology optimization.

Sato et al. [26], Yamada et al. [27], and Tajima et al. [28] developed advanced methodologies that leverage fictitious physical models to assess manufacturability. Sato et al. [26] developed a method for evaluating manufacturability in molding processes using fictitious physical models to ensure that the geometrical features of mold parts are amenable to manufacturing. Yamada et al. [27] focused on additive manufacturing and proposed a topology optimization method that addressed closed cavity exclusion constraints and enhanced the design process of additive manufacturing. Tajima et al. [28] introduced a coupled fictitious physics model aimed at improving the convergence in topology optimization by integrating the objectives of both the fictitious physical and mechanical models, particularly for additive manufacturing with geometric constraints. These methodologies collectively underscore the importance of incorporating manufacturability considerations into topology optimization, which is essential for practical applications in various manufacturing processes. The level set-based topology optimization championed by Yamada et al. [29] affords precision in modulating the geometrical intricacy of the resultant optimal configurations. Building on this foundation, Noda et al. [30] augmented this level set strategy to cater to the nuances of multi-material topology optimization. This innovation ensures a meticulous orchestration of the complexity intrinsic to each deployed material, culminating in a multi-material assembly that is conducive to straightforward manufacturing. However, the previously underscored methodologies are predominantly conceptualized for traditional, macroscopic machining techniques such as milling. Therefore, their direct application to piezoelectric energy harvesters, typically realized through microfabrication techniques such as etching [9, 31], may not be feasible.

In this study, we introduced a methodology for the optimal design of piezoelectric energy harvesters by employing topology optimization anchored in the level set method. This approach emphasizes manufacturability in the field of microfabrication, with etching being the predominant process under consideration. The design criteria for piezoelectric energy harvesters were delineated based on the operational frequency and a threshold for the excitation voltage output. Furthermore, the proposed method uniquely facilitates the concurrent optimization of three-dimensional structures within both the substrate and piezoelectric material domains. The resulting designs not only satisfy the stipulated specifications but are also readily adaptable to micro-

fabrication procedures.

The remainder of this paper is organized as follows: In Section 2, the architectural framework of the designated device is described. After this initial exposition, in this section we further elaborate on the optimal design approach, articulating the pivotal design criteria, including the eigenfrequency specifications and constraints regarding the minimum output voltage. In Section 3, we explain the formulation of constraints pertinent to manufacturability. Specifically, we introduced two constraints to enhance manufacturability: ensuring a consistent cross-sectional shape across each domain and the stipulation that no piezoelectric material is positioned without an accompanying substrate. In Section 4, implementation of the numerical analysis of the proposed method is described. In Section 5, numerical illustrations by employing a benchmark model to test the efficacy of the introduced method are detailed. Finally, in Section 6, the conclusions of this study are summarized. Additionally, the methodologies tailored for computing the output voltage are detailed in Appendix A, and the sensitivity analyses are discussed in Appendix B.

2. Formulation for the optimal design of a piezoelectric energy harvester

2.1. Unimorph cantilevered piezoelectric energy harvester

This study focused predominantly on the unimorph cantilevered energy harvester. An unimorph cantilevered piezoelectric energy harvester comprises three main components: substrate, piezoelectric material, and weight. These elements are depicted in Figure 1, which shows the theoretical structure of an unimorph cantilevered piezoelectric vibration energy harvester. The unique advantage of the unimorph design is its capability to produce a superior electrical output for a given mechanical input compared with a conventional cantilevered piezoelectric energy harvester. This superiority is attributed to the mechanical amplification effect induced by the nonpiezoelectric layer, which result in an enhanced deformation of the piezoelectric layer for a specific input vibration.

2.2. Formulation of piezoelectric phenomena

The governing equations for a piezoelectric energy harvester are articulated in the following set of simultaneous piezoelectric equations, as elaborated in [4]:

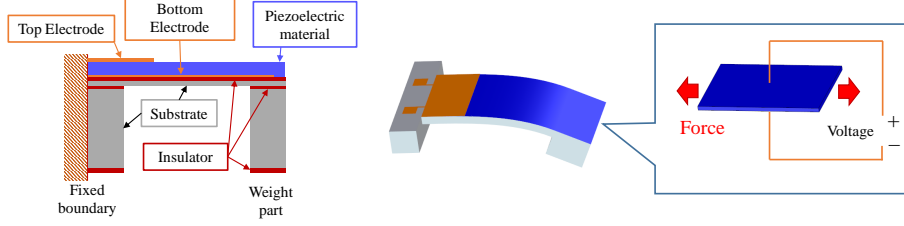


Figure 1: Concept of a piezoelectric energy harvester

$$\begin{cases} \boldsymbol{\sigma} = \mathbf{C}^E \mathbf{s}(\mathbf{u}) + \mathbf{e}^T \nabla \varphi \\ \mathbf{d} = \mathbf{e} \mathbf{s}(\mathbf{u}) + \boldsymbol{\epsilon}^S \nabla \varphi, \end{cases} \quad (1)$$

$$\mathbf{s}(\mathbf{u}) = \frac{1}{2}(\nabla \mathbf{u} + (\nabla \mathbf{u})^T). \quad (2)$$

Here, $\boldsymbol{\sigma}$ is the stress tensor; \mathbf{d} is the electric displacement tensor; \mathbf{u} is the displacement vector; $\mathbf{s}(\mathbf{u})$ represents the strain tensor; \mathbf{C}^E is the elasticity tensor at a constant electric field; and we assume that \mathbf{C}^E represents an isotropic linear elastic material; \mathbf{e} represents the piezoelectric stress constant tensor; φ is the electric potential; $\boldsymbol{\epsilon}^S$ is the dielectric constant tensor at a constant strain; and T denotes the transpose of the tensor.

In this study, we primarily focused on a piezoelectric energy harvester under harmonic excitation at a frequency ω . Within this context, the displacement vector \mathbf{u} and the electric potential φ are designated as state variables, whereas \mathbf{v} and v_φ serve as test functions. Consequently, Eq. (1) is transcribed into its weak form as follows:

$$\begin{cases} \int_{\Omega} \mathbf{s}(\mathbf{v})^T \mathbf{C}^E \mathbf{s}(\mathbf{u}) \, d\Omega - \omega^2 \rho \int_{\Omega} \mathbf{v}^T \mathbf{u} \, d\Omega + \int_{\Omega} \mathbf{s}(\mathbf{v})^T \mathbf{e}^T \nabla \varphi \, d\Omega = \int_{\Omega} \mathbf{v}^T \hat{\mathbf{f}} \, d\Omega \\ \int_{\Omega} (\nabla v_\varphi)^T \mathbf{e} \mathbf{s}(\mathbf{u}) \, d\Omega - \int_{\Omega} (\nabla v_\varphi)^T \boldsymbol{\epsilon}^S \nabla \varphi \, d\Omega = \int_{\Omega} v_\varphi \hat{\mathbf{q}} \, d\Omega. \end{cases} \quad (3)$$

Here, ρ refers to the material's density, $\hat{\mathbf{f}}$ is the external forcing function, and $\hat{\mathbf{q}}$ represents the externally provided electric charge. In this study, we assumed steady-state vibration.

The electromechanical coupling coefficient was employed as a metric to assess the performance of the piezoelectric energy harvester. The coefficient is calculated using the following equation, which considers the i -th mode eigenfrequency ω_{oci} under electrode open-circuit conditions and the i -th mode eigenfrequency ω_{sci} under electrode short-circuit conditions [32]:

$$k_i^2 = \frac{\omega_{oci}^2 - \omega_{sci}^2}{\omega_{oci}^2}. \quad (4)$$

Under open-circuit conditions (where $\hat{\mathbf{q}} = 0$), the piezoelectric simultaneous equations are expressed as follows:

$$\left\{ \begin{array}{l} \int_{\Omega} \mathbf{s}(\mathbf{v}_{oci})^T \mathbf{C}^E \mathbf{s}(\mathbf{u}_{oci}) \, d\Omega - \omega_{oci}^2 \rho \int_{\Omega} \mathbf{v}_{oci}^T \mathbf{u}_{oci} \, d\Omega + \int_{\Omega} \mathbf{s}(\mathbf{v}_{oci})^T \mathbf{e}^T \nabla \varphi_{oci} \, d\Omega = 0 \\ \int_{\Omega} \nabla v_{\varphi_{oci}}^T \mathbf{e} \mathbf{s}(\mathbf{u}_{oci}) \, d\Omega - \int_{\Omega} \nabla v_{\varphi_{oci}}^T \boldsymbol{\epsilon}^S \nabla \varphi_{oci} \, d\Omega = 0, \end{array} \right. \quad (5)$$

where \mathbf{u}_{oci} is the eigenvector corresponding to the eigenvalue ω_{oci} , φ_{oci} denotes electric potential under open-circuit condition, and \mathbf{v}_{oci} is the test function. Conversely, under short-circuit conditions (where $\nabla \varphi = 0$), the piezoelectric simultaneous equations become solely the equation for harmonic oscillation, unaffected by the influence of the piezoelectric material.

$$\int_{\Omega} \mathbf{s}(\mathbf{v}_{sci})^T \mathbf{C}^E \mathbf{s}(\mathbf{u}_{sci}) \, d\Omega - \omega_{sci}^2 \rho \int_{\Omega} \mathbf{v}_{sci}^T \mathbf{u}_{sci} \, d\Omega = 0, \quad (6)$$

where \mathbf{u}_{sci} is the eigenvector corresponding to the eigenvalue ω_{sci} and \mathbf{v}_{sci} is the test function.

In the context of piezoelectric energy harvester design, the eigenfrequency of the device is established as a crucial design parameter. Consequently, in this study, we considered strategies for concurrently aligning the eigenfrequency with the desired value. Adopting the objective function proposed by Yamada et al. [33], we normalized the eigenfrequency specification problem with respect to the i -th mode desired frequency $\bar{\omega}_i$ and formulated the

objective function F_ω as follows:

$$F_\omega = \sum_{i=1}^n \frac{|\omega_{oci} - \bar{\omega}_i|^2}{\bar{\omega}_i^2}, \quad (7)$$

where we considered F_ω as a problem specifying up to the n -th mode.

To transform the maximization problem into a minimization problem, we formulated the objective function F_k using the electromechanical coupling coefficient k_i as follows:

$$F_k = \sum_{i=1}^n \frac{1}{k_i^2 \bar{\omega}_i^2} = \sum_{i=1}^n \frac{\omega_{oci}^2}{(\omega_{oci}^2 - \omega_{sci}^2) \bar{\omega}_i^2}. \quad (8)$$

By weighting the modes by $\bar{\omega}_i$, we emphasized the lower-order modes.

In this study, we formulated an optimization problem that simultaneously minimizes distinct objective functions, that is, F_{sb} for the substrate material domain Ω_{sb} and F_{pe} for the piezoelectric material domain Ω_{pe} , while maintaining a shared state field. This formulation incorporates the weighting factors α_{sb} and α_{pe} as demonstrated below [22]:

$$\begin{aligned} \inf_{\Omega_{sb}} \quad & F_{sb} = \alpha_{sb} F_k + (1 - \alpha_{sb}) F_\omega \\ \inf_{\Omega_{pe}} \quad & F_{pe} = \alpha_{pe} F_k + (1 - \alpha_{pe}) F_\omega \\ \text{subject to} \quad & \text{governing equations for an open circuit,} \\ & \text{governing equations for a short circuit.} \end{aligned} \quad (9)$$

2.2.1. Minimum output voltage constraint

Concomitant with the eigenfrequency, the output voltage is a pivotal performance metric in the design of piezoelectric energy harvesters. This attribute is significant because devices harnessing the generated energy often require a minimum viable output voltage. Owing to the physical constitution of the piezoelectric energy harvester, wherein the piezoelectric material is encapsulated between electrodes, the resultant output voltage from the vibratory motion is closely correlated not only with the charge induced on the electrodes but also with the capacitance between the piezoelectric material and the electrodes. A larger piezoelectric material area results in a

greater charge, albeit at the cost of increased capacitance. Hence, the capacitance must be meticulously regulated to match the required output voltage. Macroscopically, the output voltage V_E is expressed as follows:

$$V_E = \frac{Q}{C_p} = \frac{\int_{\Omega_{pe}} \mathbf{n}_z \cdot \nabla \varphi \, d\Omega}{\int_{\Omega_{pe}} d\Omega / (\varepsilon_z L_z^2)}, \quad (10)$$

where C_p signifies the capacitance of the piezoelectric energy harvester, Q denotes the electrical charge elicited by the piezoelectric material, \mathbf{n}_z represents a unit vector in the polarization direction, ε_z is the polarization direction component of the piezoelectric material's dielectric constant tensor, and L_z is the thickness of the piezoelectric domain. The constraint on the minimum output voltage is formulated as follows:

$$V_E = \frac{\int_{\Omega_{pe}} \mathbf{n}_z \cdot \nabla \varphi \, d\Omega}{\int_{\Omega_{pe}} d\Omega / (\varepsilon_z L_z^2)} \geq \bar{V}_{minV}, \quad (11)$$

$$\int_{\Omega_{pe}} d\Omega \leq \frac{\varepsilon_z L_z^2 \int_{\Omega_{pe}} \mathbf{n}_z \cdot \nabla \varphi \, d\Omega}{\bar{V}_{minV}}, \quad (12)$$

where \bar{V}_{minV} denotes the minimum output voltage. This formulation allows the minimum output voltage constraint to be treated similarly to the volume constraint.

2.3. Concept of topology optimization

Topology optimization is a type of structural optimization method. Structural optimization is used to obtain a structure Ω that minimizes or maximizes an objective function. The objective function often includes physical properties, such as stiffness [11, 34], as well as thermal [35, 36, 37, 38, 39], fluid [40, 41], electromagnetic [42, 43], and acoustic properties [44, 45, 46, 47]. Therefore, the optimal structure is obtained under the assumption that the objective function satisfies the governing equations that describe the physical phenomena. The governing equations are considered as constraints in the optimization problem, and the basic structural optimization problem can be formulated as follows:

$$\begin{aligned} \inf_{\Omega} \quad & F(u, \Omega) = \int_{\Omega} f(u) d\Omega \\ \text{subject to} \quad & \text{the governing equation system,} \\ & \text{constraint equations,} \end{aligned} \quad (13)$$

where u is the state variable obtained as the solution of the governing equation and $f(u)$ is the objective function.

Next, we considered the application of topology optimization to the structural optimization problem (13). We introduced a domain $\Omega_D \subset \mathbb{R}^n$ ($n = 2$ or 3) where the structure can be placed. Here, the domain Ω_D is called a fixed design domain because it does not change during the optimization process. The fixed design domain consists of a domain filled with the structure (hereafter referred to as the material domain) and a domain not filled with the structure (hereafter referred to as the void domain), and these domains are expressed by the characteristic function χ , which is defined as follows:

$$\chi(\mathbf{x}) := \begin{cases} 1 & \text{for } \mathbf{x} \in \Omega \\ 0 & \text{for } \mathbf{x} \in \Omega_D \setminus \Omega, \end{cases} \quad (14)$$

where the boundary between the material and void domains is included in the material domain. Using the characteristic function χ , the topology optimization problem can be formulated as follows:

$$\begin{aligned} \inf_{\chi} \quad & F(u, \chi) = \int_{\Omega_D} f(u) \chi d\Omega \\ \text{subject to} \quad & \begin{aligned} & \text{the governing equation system,} \\ & \text{constraint equations.} \end{aligned} \end{aligned} \quad (15)$$

In topology optimization, the problem described in (13) is reformulated as a material-distribution problem. This allows for topological changes, such as an increase or decrease in the number of holes, during the optimization procedure.

However, topology optimization problems are commonly ill-posed [34]; therefore, the space of admissible design should incorporate relaxation or regularization techniques to render the problem well-posed. A typical method based on the relaxation of space of an admissible design is the homogenization method [11]. In this study, we used a level set-based topology optimization method [29] to transform an ill-posed problem into a well-posed problem. In this method, the boundary surface of the material domain is represented by the isosurface of a scalar function called the level set function, and changes in the level set function represent changes in the shape of the material domain. The topology optimization problem is regularized by ensuring the proper smoothness of the level set function. This method is described in subsection 2.3.1.

2.3.1. Level set-based topology optimization

In the level set-based method, the scalar function $\phi(\mathbf{x}) \in H^1(\Omega_D)$, also called the level set function, illustrated in the following equation is introduced to represent the shape:

$$\begin{cases} -1 \leq \phi(\mathbf{x}) < 0 & \text{for } \mathbf{x} \in \Omega_D \setminus \Omega \\ \phi(\mathbf{x}) = 0 & \text{for } \mathbf{x} \in \partial\Omega \\ 1 \geq \phi(\mathbf{x}) > 0 & \text{for } \mathbf{x} \in \Omega, \end{cases} \quad (16)$$

where $\partial\Omega$ denotes the boundaries between the material and void domains. We redefined the characteristic function using the level set function as follows:

$$\chi_\phi(\phi(\mathbf{x})) := \begin{cases} 1 & \text{for } \phi(\mathbf{x}) \geq 0 \\ 0 & \text{for } \phi(\mathbf{x}) < 0. \end{cases} \quad (17)$$

In the level set-based method, the topology optimization problem is formulated using the characteristic function defined in (17). However, as previously discussed, optimization that employs characteristic functions as design variables constitutes an ill-posed problem. Consequently, the level set-based method offers regularization to this optimization challenge, which is formulated as follows:

$$\begin{aligned} \inf_{\phi} \quad & F_R(u, \phi) = \int_{\Omega_D} f(u) \chi_\phi(\phi) d\Omega + \int_{\Omega_D} \frac{1}{2} \tau |\nabla \phi|^2 d\Omega \\ \text{subject to} \quad & \text{the governing equation system,} \\ & \text{constraint equations,} \end{aligned} \quad (18)$$

where $\tau \in \mathbb{R}_+$ is the regularization coefficient.

Next, we describe a method for updating the level set function. Assuming that the level set function is a function of fictitious time t , it is updated by the reaction-diffusion equation as follows:

$$\begin{aligned} \frac{\partial \phi(\mathbf{x}, t)}{\partial t} &= -K(\phi) \{ -\tilde{c} F' - \tau \nabla^2 \phi(\mathbf{x}, t) \}, \\ \tilde{c} &:= \frac{c \int_{\Omega_D} d\Omega}{\int_{\Omega_D} |F'| d\Omega}, \end{aligned} \quad (19)$$

where $K \in \mathbb{R}_+$ is the proportionality coefficient, $c \in \mathbb{R}_+$ is the normalization coefficient, and F' is the design sensitivity. In this study, we set $K = 1.0$ and $c = 2.0$.

3. Formulation of constraints for manufacturability

In this section, we describe the formulation of prerequisites related to manufacturing processes. This study set forth specific manufacturing criteria for piezoelectric energy harvesters, emphasizing configurations amenable to etching methodologies, predominantly utilizing the deep reactive ion etching (DRIE) apparatus [9] [48]. To this end, constraints were introduced to ensure structural uniformity in the thickness direction for both the piezoelectric and substrate domains. Such constraints prevent the emergence of configurations with apertures oriented in oblique or orthogonal directions relative to the processing trajectory. In addition, we advocated the imposition of a substrate-dependent constraint on the piezoelectric domain, precluding the occurrence of piezoelectric materials in areas devoid of a substrate. This constraint ensures that the piezoelectric materials do not exist in areas where the substrate is absent. The intricacies of each constraint are described below.

3.1. Constraint: the same cross-sectional shape in each domain

Within the framework of topology optimization obtained via the level set method, qualitative control over complexity can be regulated by the regularization coefficient τ , as defined in Eq. (18) [29]. To leverage this control over complexity, we propose strategies to assign regularization coefficients that curtail the complexity in the thickness direction of the structure, thereby facilitating manufacturability via etching. We provided the regularization coefficient as a tensor $\boldsymbol{\tau}$, and modified Eq. (19) as follows:

$$\frac{\partial \phi(\mathbf{x}, t)}{\partial t} = -K(\phi) \left\{ -\tilde{c}F' - \nabla^T \boldsymbol{\tau} \nabla \phi(\mathbf{x}, t) \right\}, \quad (20)$$

where

$$\boldsymbol{\tau} = \begin{bmatrix} \tau_x & 0 & 0 \\ 0 & \tau_y & 0 \\ 0 & 0 & \tau_z \end{bmatrix}. \quad (21)$$

In this context, augmenting the component of the regularization coefficient tensor associated with the gradient in a specific direction of the level set function simplifies the complexity along that direction. By defining the thickness direction as z and assigning $\tau_x, \tau_y \ll \tau_z$, we can obtain a structure exhibiting

minimal complexity in the thickness direction, thus enhancing manufacturability via etching.

Although the method described above controls the complexity of the structure throughout the design domain, the substrate and piezoelectric components can be readily processed via etching, even if their structures differ. It is desirable to control the complexity in the thickness direction within the substrate and piezoelectric domains without affecting the structural differences at the interface of each domain. To this end, in this study, we defined separate level set functions for the substrate and piezoelectric structures, invoking the extended level set method [30], which is capable of handling multiple materials and updating each level set function concurrently. The fixed design domains for the substrate and piezoelectric material are denoted as D_{sb} and D_{pe} , respectively, assuming that these domains remain invariant throughout the optimization procedure. The fixed design domain, denoted as D , encompasses both D_{pe} and D_{sb} . Within the fixed design domain D , two distinct level set functions ϕ_{pe} and ϕ_{sb} along with characteristic functions χ_{ps} and χ_{sp} signifying the respective domains are defined as follows:

$$\begin{cases} 0 < \phi_{pe}(\mathbf{x}) \leq 1 & \text{if } \mathbf{x} \in \Omega_{pe} \\ \phi_{pe}(\mathbf{x}) = 0 & \text{if } \mathbf{x} \in \partial\Omega_{pe} \cup D_{sb} \\ -1 \leq \phi_{pe}(\mathbf{x}) < 0 & \text{if } \mathbf{x} \in D_{pe} \setminus \Omega_{pe}, \end{cases} \quad (22)$$

$$\begin{cases} 0 < \phi_{sb}(\mathbf{x}) \leq 1 & \text{if } \mathbf{x} \in \Omega_{sc} \\ \phi_{sb}(\mathbf{x}) = 0 & \text{if } \mathbf{x} \in \partial\Omega_{sc} \cup D_{pe} \\ -1 \leq \phi_{sb}(\mathbf{x}) < 0 & \text{if } \mathbf{x} \in D_{sb} \setminus \Omega_{sb}, \end{cases} \quad (23)$$

$$\begin{cases} \chi_{ps} = 1 & \text{in } D_{pe} \\ \chi_{ps} = 0 & \text{in } D_{sb}, \end{cases} \quad (24)$$

$$\begin{cases} \chi_{sp} = 0 & \text{in } D_{pe} \\ \chi_{sp} = 1 & \text{in } D_{sb}. \end{cases} \quad (25)$$

Each level set function for the piezoelectric and substrate domains is updated as follows:

$$\frac{\partial \phi_{pe}}{\partial t} = -K(-\tilde{c}F'_{pe} - \nabla(\boldsymbol{\tau}_p \nabla \phi_{pe})), \quad (26)$$

$$\frac{\partial \phi_{sb}}{\partial t} = -K(-\tilde{c}F'_{sb} - \nabla(\boldsymbol{\tau}_{sb} \nabla \phi_{sb})), \quad (27)$$

where F'_{pe} is the gradient of the objective function F_{pe} with respect to ϕ_{pe} ; F'_{sb} is the gradient of the objective function F_{sb} with respect to ϕ_{sb} ; and $\boldsymbol{\tau}_{pe}$ and $\boldsymbol{\tau}_{sb}$ are the regularization factor tensors for ϕ_{pe} and ϕ_{sb} , respectively. By individually defining the regularization coefficient tensors for the piezoelectric and substrate domains, the complexity in the thickness direction for each domain can be controlled, thereby enhancing the manufacturability.

3.2. Constraint: no piezoelectric material is placed without a substrate

Herein, we elucidate an approach that allows the imposition of geometric constraints using a fictitious physical function field denoted by p . The concept of fictitious physical models described by a steady-state anisotropic advection-diffusion equation was initially introduced by Sato et al. [26]. A further elaboration of the fictitious physical model using the anisotropic diffusion equation was provided by Yamada et al. [27], which is described below.

$$\begin{aligned} -\operatorname{div}(\boldsymbol{\kappa}_p \nabla p) + \chi_{sp}(p - \bar{p}_s(2\chi(\phi_{sb}) - 1)) &= 0 & \text{in } D, \\ p &= -\bar{p}_0 & \text{on } \Gamma_p, \\ \nabla p \cdot \mathbf{n} &= 0 & \text{on } \partial D \setminus \Gamma_p, \end{aligned} \quad (28)$$

$$\boldsymbol{\kappa}_p = \begin{bmatrix} \kappa_x & 0 & 0 \\ 0 & \kappa_y & 0 \\ 0 & 0 & \kappa_z \end{bmatrix}, \quad (29)$$

where $\boldsymbol{\kappa}_p$ represents the conductivity tensor of p ; κ_x , κ_y , and κ_z represent the anisotropic conductivities along the x , y , and z directions, respectively; and $\bar{p}_s \in \mathbb{R}_+$ and $\bar{p}_0 \in \mathbb{R}_+$ are the constants for the generation and boundary conditions of p . In this study, the thickness direction was represented by the z -axis, which was employed as a constraint to determine the presence or absence of the substrate. The anisotropic conductivities κ_x and κ_y were set to values substantially lower than κ_z . The boundary Γ_p , subjected to the Dirichlet boundary condition, was identified as the boundary opposite to domain D_{pe} within the domain D_{sb} . The second term in the initial equation of (28) ensures that $p = \bar{p}_s$ within the substrate material domain Ω_{sb} . Within the substrate material domain Ω_{sb} , the fictitious heat p is generated and propagated in the z -direction towards the domain D_{pe} when a material is

present within Ω_{sb} . Conversely, in the absence of a material in Ω_{sb} , the boundary condition $p = -p_0$ is conveyed to the domain D_{pe} owing to the lack of p generation in Ω_{sb} .

3.3. Formulation of the optimal design with proposed constraints

By incorporating the aforementioned methodologies, the optimal design problem is formulated as follows:

$$\begin{aligned}
& \inf_{\phi_{pe}} && F_{pe}(\omega_{oc}, \omega_{sc}) \\
& \inf_{\phi_{sb}} && F_{sb}(\omega_{oc}, \omega_{sc}) \\
\text{subject to} &&& a_{oc}(\phi_{pe}, \phi_{sb}, \omega_{oc}, \mathbf{u}_{oc}, \mathbf{v}_{oc}, \varphi_{oc}, p) = 0, \\
&&& b_{oc}(\phi_{pe}, \phi_{sb}, \mathbf{u}_{oc}, \varphi_{oc}, v_{\varphi_{oc}}, p) = 0, \\
&&& a_{sc}(\phi_{pe}, \phi_{sb}, \omega_{sc}, \mathbf{u}_{sc}, \mathbf{v}_{sc}, p) = 0, \\
&&& a_p(\phi_{pe}, \phi_{sb}, p, v_p) = 0, \\
&&& G_V(\phi_{pe}, \varphi_{oc}) \leq 0,
\end{aligned} \tag{30}$$

$$\begin{aligned}
& a_{oc}(\phi_{pe}, \phi_{sb}, \omega_{oc}, \mathbf{u}_{oc}, \mathbf{v}_{oc}, \varphi_{oc}) \\
&= \left(\int_{\Omega_{pe}} \mathbf{s}(\mathbf{v}_{oc})^T \mathbf{C}_{pe}^E \mathbf{s}(\mathbf{u}_{oc}) \, d\Omega - \omega_{oc}^2 \int_{\Omega_{pe}} \rho_{pe} \mathbf{v}_{oc}^T \mathbf{u}_{oc} \, d\Omega \right. \\
&\quad \left. + \int_{\Omega_{pe}} \mathbf{s}(\mathbf{v}_{oc})^T \mathbf{e}^T \nabla \varphi_{oc} \, d\Omega \right) \\
&\quad + \left(\int_{\Omega_{sb}} \mathbf{s}(\mathbf{v}_{oc})^T \mathbf{C}_{sb}^E \mathbf{s}(\mathbf{u}_{oc}) \, d\Omega - \omega_{oc}^2 \int_{\Omega_{sb}} \rho_{sb} \mathbf{v}_{oc}^T \mathbf{u}_{oc} \, d\Omega \right) = 0,
\end{aligned} \tag{31}$$

$$\begin{aligned}
& b_{oc}(\phi_{pe}, \phi_{sb}, \mathbf{u}_{oc}, \varphi_{oc}, v_{\varphi_{oc}}) \\
&= \int_{\Omega_{pe}} \nabla v_{\varphi_{oc}}^T \mathbf{e} \mathbf{s}(\mathbf{u}_{oc}) \, d\Omega - \int_{\Omega_{pe}} \nabla v_{\varphi_{oc}}^T \boldsymbol{\varepsilon}^S \nabla \varphi_{oc} \, d\Omega = 0,
\end{aligned} \tag{32}$$

$$\begin{aligned}
& a_{sc}(\phi_{pe}, \phi_{sb}, \omega_{sc}, \mathbf{u}_{sc}, \mathbf{v}_{sc}) \\
&= \left(\int_{\Omega_{pe}} \mathbf{s}(\mathbf{v}_{sc})^T \mathbf{C}_{pe}^E \mathbf{s}(\mathbf{u}_{sc}) \, d\Omega - \omega_{sc}^2 \int_{\Omega_{pe}} \rho_{pe} \mathbf{v}_{sc}^T \mathbf{u}_{sc} \, d\Omega \right) \\
&\quad + \left(\int_{\Omega_{sb}} \mathbf{s}(\mathbf{v}_{sc})^T \mathbf{C}_{sb}^E \mathbf{s}(\mathbf{u}_{sc}) \, d\Omega - \omega_{sc}^2 \int_{\Omega_{sb}} \rho_{sb} \mathbf{v}_{sc}^T \mathbf{u}_{sc} \, d\Omega \right) = 0,
\end{aligned} \tag{33}$$

$$a_p(\phi_{pe}, \phi_{sb}, p, v_p) = \int_D \nabla v_p \boldsymbol{\kappa}_p \nabla p \, d\Omega + \int_D \chi_{sp} (p - \bar{p}_s (2\chi(\phi_{sb}) - 1)) v_p \, d\Omega = 0, \tag{34}$$

$$G_V(\phi_{pe}, \varphi) = \int_{\Omega_{pe}} d\Omega - \frac{\varepsilon_z L_z^2 \int_{\Omega_{pe}} \mathbf{n}_z \cdot \nabla \varphi \, d\Omega}{\bar{V}_{minV}} \leq 0, \tag{35}$$

where \mathbf{C}_{pe}^E and \mathbf{C}_{sb}^E are the elastic tensors of the piezoelectric and substrate materials, respectively. Similarly, ρ_{pe} and ρ_{sb} represent the densities of the piezoelectric and substrate materials, respectively. Additionally, v_p acts as a test function for the fictitious physical function p . The potential, symbolized by φ , is obtained from the displacement \mathbf{u} derived via the modal superposition method. This is distinct from φ_{oc} , which is determined based on the eigenvector \mathbf{u}_{oc} . A comprehensive exposition on the derivation of the potential φ through the modal superposition method can be found in Appendix A.

4. Numerical implementation

4.1. Optimization algorithm

The optimization algorithm is implemented as follows:

- Step 1:** The initial level set function is set.
- Step 2:** The fictitious physical function field p based on Eq. (34) is solved using the finite element method (FEM).
- Step 3:** The eigenvector fields \mathbf{u}_{oc} and \mathbf{u}_{sc} and eigenvalues ω_{oc} , ω_{sc} , and φ_{oc} derived from Eqs. (31)–(33) are solved using the FEM.
- Step 4:** The objective functions F_{pe} and F_{sb} derived from Eq. (9) together with the output voltage V_E at a frequency $\bar{\omega}_i$ and the constraint function G_V , which is based on Eq. (35), are evaluated.
- Step 5:** If the objective functions converge, the optimization procedure is terminated; otherwise, the sensitivity with respect to the objective functions is computed.
- Step 6:** The level set function is updated using the time evolution equation given by Eq. (19), and the optimization procedure returns to step 2.

FreeFEM++ [49] was used as the FEM solver. In the following subsections, we explain the approximations of the displacement and electrical potential fields and the sensitivity analysis.

4.2. Approximate solution of the displacement and electrical potential fields based on the Eulerian coordinate system

Within the Eulerian coordinate system, the fixed design domain necessitates the generation of finite elements during each iteration of the optimization process. To mitigate the computational expenditure, an ersatz material approach, as delineated in [50], was employed. In particular, the void domain was assumed to be a structural material with a relatively small elastic tensor, and the material properties were assumed to be smoothly distributed in the vicinity of the interface. The governing equations, which dictate the displacement field within the FEM, originally pertain to the material domain Ω_D . Utilizing the level set, characteristic, and fictitious physical functions delineated in Section 3, coupled with an approximated Heaviside function $h(\phi)$

to be presented subsequently, we extended these equations to encompass the entire fixed design domain D as follows:

$$\begin{aligned} \chi(\phi) &\approx h(\phi), \\ h(\phi) &:= \begin{cases} d & \text{for } \phi < -w \\ \left\{ \frac{1}{2} + \frac{\phi}{w} \left[\frac{15}{16} - \frac{\phi^2}{w^2} \left(\frac{5}{8} - \frac{3}{16} \frac{\phi^2}{w^2} \right) \right] \right\} (1-d) + d & \text{for } -w \leq \phi \leq w, \\ 1 & \text{for } w < \phi \end{cases} \end{aligned} \quad (36)$$

$$\mathbf{C}_{\phi ps}^E := \mathbf{C}_{pe}^E \chi_{ps} h(\phi_{pe}) h(p) + \mathbf{C}_{sb}^E \chi_{sp} h(\phi_{sb}), \quad (37)$$

$$\mathbf{e}_{\phi ps} := \mathbf{e}_{\chi ps} h(\phi_{pe}) h(p), \quad (38)$$

$$\boldsymbol{\varepsilon}_{\phi ps}^S := \varepsilon_0 \mathbf{I} (1 - (\chi_{ps} h(\phi_{pe}) h(p) + \chi_{sp} h(\phi_{sb}))) + \boldsymbol{\varepsilon}^S \chi_{ps} h(\phi_{pe}) h(p), \quad (39)$$

$$\rho_{\phi ps} := \rho_{pe} \chi_{ps} h(\phi_{pe}) h(p) + \rho_{sb} \chi_{sp} h(\phi_{sb}), \quad (40)$$

where $\mathbf{C}_{\phi ps}^E$ is the extended elastic tensor, $\mathbf{e}_{\phi ps}$ is the extended piezoelectric constant tensor, $\boldsymbol{\varepsilon}_{\phi ps}^S$ is the extended permittivity tensor, $\rho_{\phi ps}$ is the extended density, w is the transition width of the Heaviside function, and d is a sufficiently small positive number. In this study, we set $w = 0.9$ and $d = 0.01$.

4.3. Sensitivity analysis

Here, we describe a procedure for determining the sensitivity to update level set functions. In this study, based on Eqs. (31)–(35), we defined Lagrangian L_{pe} and L_{sb} with respect to ϕ_{pe} and ϕ_{sb} , respectively, as follows:

$$\begin{aligned} L_{pe} = & F_{pe}(\omega_{oc}, \omega_{sc}) + a_{oc}(\phi_{pe}, \phi_{sb}, \omega_{oc}, \mathbf{u}_{oc}, \mathbf{v}_{ocpe}, \varphi_{oc}) + b_{oc}(\phi_{pe}, \phi_{sb}, \mathbf{u}_{oc}, \varphi_{oc}, v_{\varphi_{ocpe}}) \\ & + a_{sc}(\phi_{pe}, \phi_{sb}, \omega_{sc}, \mathbf{u}_{sc}, \mathbf{v}_{scpe}) + a_p(\phi_{pe}, \phi_{sb}, p, v_p) + \lambda G_V(\phi_{pe}, \varphi_{oc}), \end{aligned} \quad (41)$$

$$\begin{aligned} L_{sb} = & F_{sb}(\omega_{oc}, \omega_{sc}) + a_{oc}(\phi_{pe}, \phi_{sb}, \omega_{oc}, \mathbf{u}_{oc}, \mathbf{v}_{ocsb}, \varphi_{oc}) + b_{oc}(\phi_{pe}, \phi_{sb}, \mathbf{u}_{oc}, \varphi_{oc}, v_{\varphi_{ocsb}}) \\ & + a_{sc}(\phi_{pe}, \phi_{sb}, \omega_{sc}, \mathbf{u}_{sc}, \mathbf{v}_{scsb}) + a_p(\phi_{pe}, \phi_{sb}, p, v_p), \end{aligned} \quad (42)$$

where \mathbf{v}_{ocpe} , \mathbf{v}_{ocsb} , \mathbf{v}_{sc} , \mathbf{v}_{scpe} , \mathbf{v}_{scsb} , $v_{\varphi_{ocpe}}$, $v_{\varphi_{ocsb}}$, and λ are the Lagrange multipliers. Using the adjoint method, sensitivity was determined as follows:

$$\begin{aligned} F'_{pe} = & c_{ocpe} \{ a_{oc}(1, \phi_{sb}, \omega_{oc}, \mathbf{u}_{oc}, \mathbf{u}_{oc}, \varphi_{oc}) + b_{oc}(1, \mathbf{u}_{oc}, \varphi_{oc}, \varphi_{oc}) \} \\ & + c_{scpe} a_{sc}(1, \phi_{sb}, \omega_{sc}, \mathbf{u}_{sc}, \mathbf{u}_{sc}) + \lambda, \end{aligned} \quad (43)$$

$$\begin{aligned} F'_{sb} = & c_{ocsb} \{ a_{oc}(\phi_{pe}, 1, \omega_{oc}, \mathbf{u}_{oc}, \mathbf{u}_{oc}, \varphi_{oc}) \} \\ & + c_{scsb} \{ a_{sc}(\phi_{pe}, 1, \omega_{sc}, \mathbf{u}_{sc}, \mathbf{u}_{sc}) \}. \end{aligned} \quad (44)$$

The sensitivity analysis is explained in detail in Appendix B.

5. Numerical examples

In this section, several numerical examples are presented to demonstrate the utility and validity of the proposed method.

The design domain and associated boundary conditions are illustrated in Figure 2. Let D_{pe} denote a square, colored in blue in the figure, with a side length of 500 mm and a thickness of 4 mm. The object in this domain was a piezoelectric material. Similarly, let D_{sb} symbolize a square, indicated in grey in the figure, with a side length of 500 mm and a thickness of 36 mm. The object within this domain did not exhibit any piezoelectric properties. The domain measuring 500 mm in length, 20 mm in width, and 36 mm in thickness, depicted in dark purple in the figure, was a nondesigned domain inhabited by a nonpiezoelectric material. Correspondingly, the domain that is 500 mm in length, 20 mm in breadth, and 4 mm in thickness, illustrated in light purple in the figure, represents a nondesigned domain occupied by a piezoelectric material. A fixed boundary condition was imposed on the surfaces adjacent to as well as the opposite domain D_{sb} . The domain colored red on the right side of the figure, delineating a 20-mm square with a thickness of 40 mm, is designated as the weight domain, which is a nondesigned domain filled with objects devoid of piezoelectric properties. The density was assumed to be 100 times that of the substrate material within this weight domain. The number of modes to be contemplated was fixed at $n = 4$, and the specified natural frequencies were $[\bar{\omega}_0, \bar{\omega}_1, \bar{\omega}_2, \bar{\omega}_3] = [70 \text{ Hz}, 435 \text{ Hz}, 450 \text{ Hz}, 500 \text{ Hz}]$. The initial structure was conjectured to be such that $\phi_{pe} = 1$ in D_{pe} and $\phi_{sb} = 1$ in D_{sb} , indicating that the entire fixed design domain was occupied by the material domain.

5.1. Effectiveness of the proposed constraints for manufacturability

We conducted numerical experiments under nine conditions, as listed in Table 1. Each condition was characterized by a distinct setting of the regularization factor τ_z in the thickness direction, the representation of level set functions (either a singular function ϕ or a pair of functions ϕ_{pe} and ϕ_{sb}), and the status of constraint implementation via a fictitious field p . Specifically, for each condition, the regularization factor τ_z was set to 1.0×10^{-6} , 1.0×10^{-4} , or 1.0×10^{-2} . Furthermore, the level set functions were either represented solely by ϕ or by a combination of ϕ_{pe} and ϕ_{sb} , and the constraints

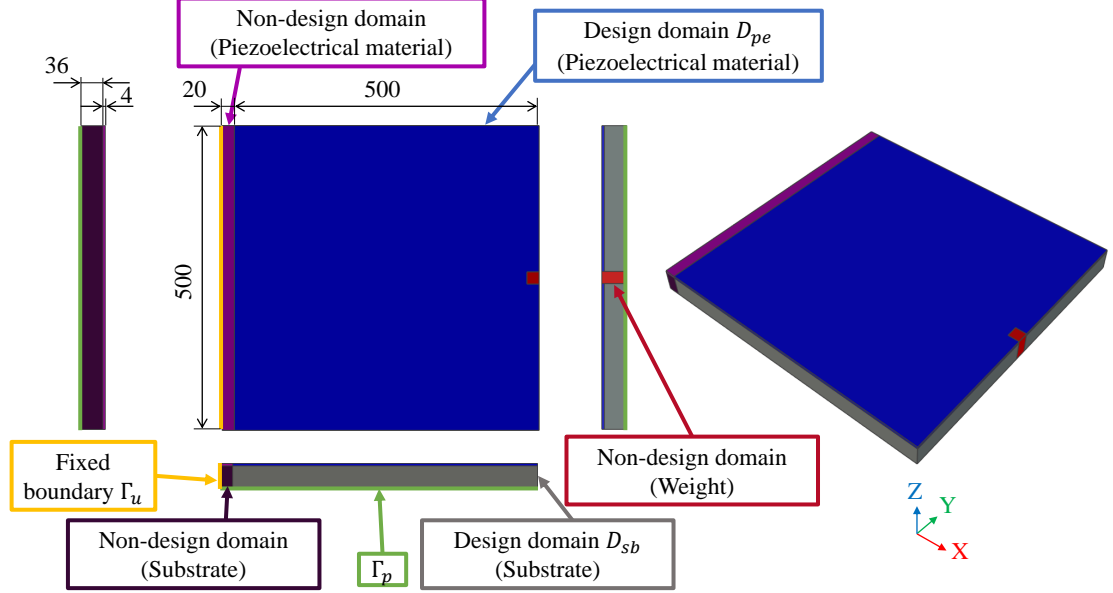


Figure 2: Design domain and boundary conditions.

were applied using the fictitious field p for some conditions. Each of these nine configurations was evaluated through 1000 iterations of computation. The parameters corresponding to each condition, coupled with the average values of the objective function F_k and F_ω taken over the last 100 iterations, are also presented in Table 1. Under all conditions, α_{pe} and α_{sb} were set to 0.95. The resulting structures for each condition are shown in Figure 3.

The tradeoff relationship between the objective functions F_k and F_ω for conditions (a)–(i) delineated in Table 1 is depicted in Figure 4. From the figure, a clear tradeoff relationship can be discerned between F_ω and F_k , the balance of which is influenced by changes in the parameter τ_z . Moreover, conditions (d)–(f) yielded smaller F_k values than conditions (a)–(c), given the same τ_z value. This phenomenon is attributed to the fact that, in conditions (d)–(f), the architecture of the piezoelectric film remained uninfluenced by the structure of the substrate, and, apart from regularization with respect to ϕ_{pe} , it does not adhere to any constraints. This allows for a wider variety of potential solutions, thereby enhancing the structural degrees of freedom of piezoelectric films. In conditions (g)–(i), although the structure of the piezoelectric film was influenced by the structure of the substrate, the converse does not hold true, resulting in F_ω values that are lower than those under

Table 1: Summary of parameter settings and objective functions: regularization factor τ_z in the thickness direction, the representation of level set functions, and the status of constraint implementation via a fictitious field p and the corresponding objective functions F_k and F_ω for each condition.

condition	τ_z	level set function	p constraint	Objective function	
				F_k	F_ω
(a)	1.0×10^{-6}	ϕ	not constrained	4.47×10^{-5}	1.52×10^{-5}
(b)	1.0×10^{-4}	ϕ	not constrained	7.07×10^{-5}	6.70×10^{-6}
(c)	1.0×10^{-2}	ϕ	not constrained	8.43×10^{-5}	4.98×10^{-6}
(d)	1.0×10^{-6}	ϕ_{pe} and ϕ_{sb}	not constrained	4.50×10^{-5}	1.51×10^{-5}
(e)	1.0×10^{-4}	ϕ_{pe} and ϕ_{sb}	not constrained	5.80×10^{-5}	1.33×10^{-5}
(f)	1.0×10^{-2}	ϕ_{pe} and ϕ_{sb}	not constrained	7.20×10^{-5}	1.08×10^{-5}
(g)	1.0×10^{-6}	ϕ_{pe} and ϕ_{sb}	p constrained	4.70×10^{-5}	1.25×10^{-5}
(h)	1.0×10^{-4}	ϕ_{pe} and ϕ_{sb}	p constrained	4.53×10^{-5}	1.28×10^{-5}
(i)	1.0×10^{-2}	ϕ_{pe} and ϕ_{sb}	p constrained	8.14×10^{-5}	4.79×10^{-6}

conditions (d)–(f).

For each condition, we computed two normalized quantities: $N_{\phi 1}$ and $N_{\phi 2}$. $N_{\phi 1}$ is the proportion of nodes at which the product of the level set functions with their adjacent nodes in the z-negative direction is negative, suggesting a boundary with the adjacent nodes. Conversely, $N_{\phi 2}$ is the proportion of nodes not located at the boundaries of domains D_{sb} and D_{pe} . These values were normalized by the total number of nodes. The computed values for $N_{\phi 1}$ and $N_{\phi 2}$ for each condition are provided in Table 2.

As delineated in Table 2, irrespective of the level set function configuration and the existence of a p constraint, an increase in the τ_z value corresponded to a reduction in the z-directional complexity. When two level set functions were utilized, as in conditions (d)–(i), the $N_{\phi 1}$ value surpassed that in conditions (a)–(c), where a single level set function embodied the entirety of the design domain. Contrastingly, $N_{\phi 2}$, excluding the interface between D_{sb} and D_{pe} , did not exhibit a significant difference from $N_{\phi 1}$ under conditions (a)–(c) but was less than $N_{\phi 1}$ in conditions (d)–(i). This phenomenon can be attributed to the fact that, when two level set functions are employed, the structural complexity is not restrained at the boundary between domains D_{sb} and D_{pe} , even upon altering the τ_z value. Hence, the $N_{\phi 1}$ value was considered higher than that in conditions (a)–(c).

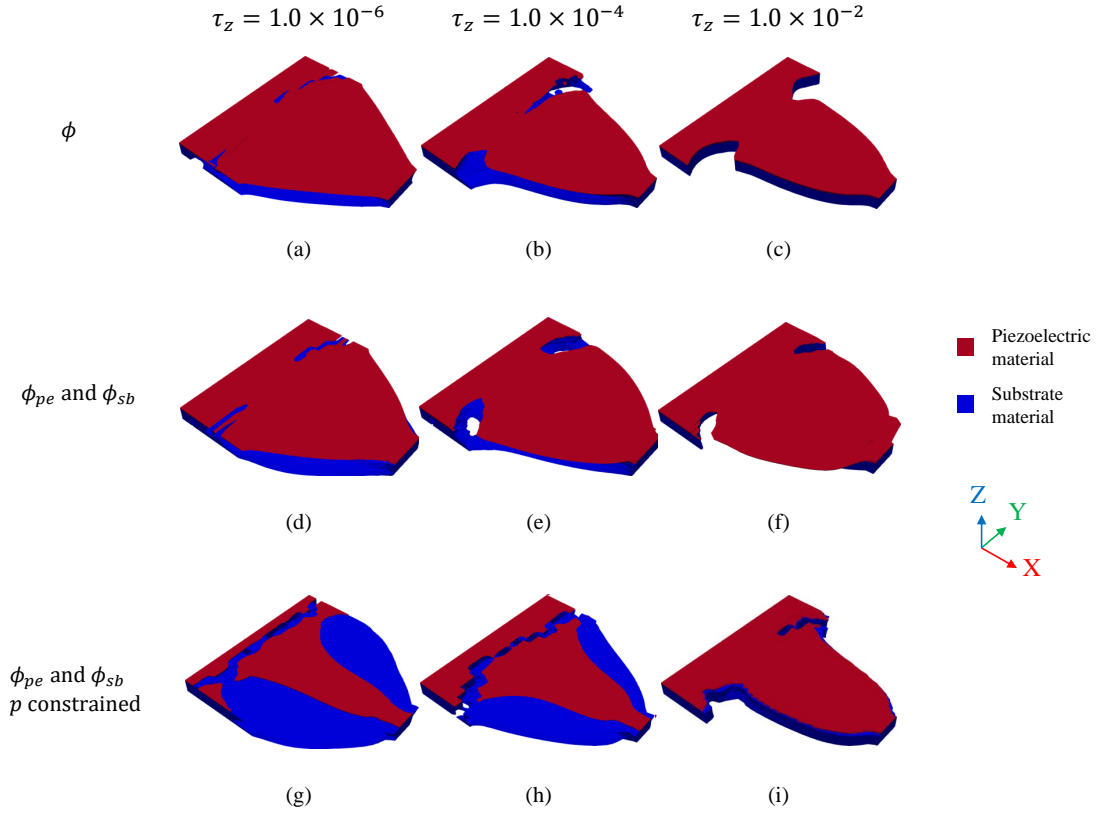


Figure 3: Optimal configuration of an unimorph cantilevered energy harvester for conditions (a)–(i) listed in Table 1. The red region denotes the piezoelectric material domain Ω_{pe} , and the blue region represents the substrate material domain Ω_{sb} .

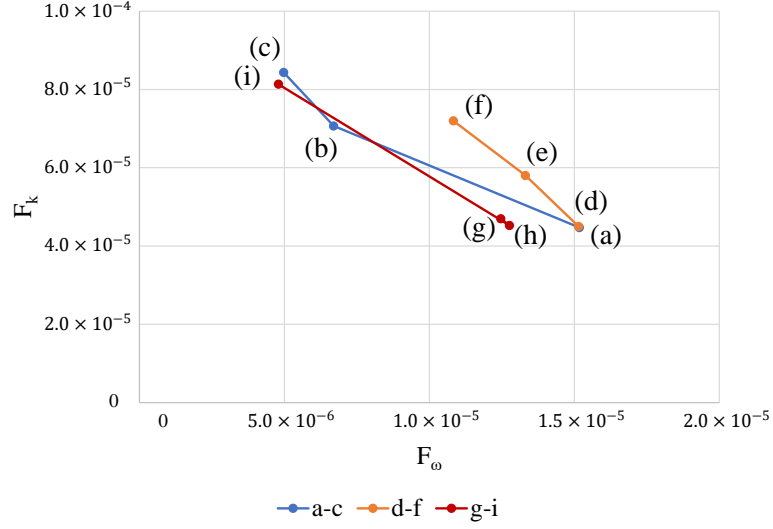


Figure 4: Tradeoff relationship between the objective functions F_k and F_ω under conditions (a)–(i) listed in Table 1.

Table 2: Number of nodes where the product of their level set function values with nodes adjacent to the negative direction of the z-axis is negative for each condition

condition	τ_z	$N_{\phi 1}$	$N_{\phi 2}$
(a)	1.0×10^{-6}	0.08818	0.07629
(b)	1.0×10^{-4}	0.01965	0.01819
(c)	1.0×10^{-2}	0.00049	0.00042
(d)	1.0×10^{-6}	0.08890	0.07138
(e)	1.0×10^{-4}	0.05058	0.03523
(f)	1.0×10^{-2}	0.01898	0.00079
(g)	1.0×10^{-6}	0.14124	0.10782
(h)	1.0×10^{-4}	0.08660	0.06932
(i)	1.0×10^{-2}	0.00340	0.00200

Table 3: Summary of constraint parameters and objective functions: minimum output voltage constraint \bar{V}_{minV} and the corresponding objective functions F_k and F_ω , the output voltage V_E , and the volume of piezoelectric material domain Ω_{pe} for each condition.

condition	Constraint \bar{V}_{minV}	Objective function F_k F_ω		Output voltage V_E	Volume of Ω_{pe} V_{pe}
(j)	9.0×10^{-3}	8.44×10^{-5}	4.56×10^{-6}	9.73×10^{-3}	4.47×10^5
(k)	9.5×10^{-3}	1.82×10^{-4}	4.87×10^{-6}	9.50×10^{-3}	2.31×10^5
(l)	1.0×10^{-2}	2.03×10^{-4}	5.60×10^{-6}	1.00×10^{-2}	2.07×10^5
(m)	1.05×10^{-2}	2.21×10^{-4}	6.23×10^{-6}	1.05×10^{-2}	1.90×10^5
(n)	1.1×10^{-2}	2.34×10^{-4}	6.72×10^{-6}	1.10×10^{-2}	1.80×10^5
(o)	1.15×10^{-2}	2.45×10^{-4}	7.11×10^{-6}	1.15×10^{-2}	1.71×10^5
(p)	1.2×10^{-2}	2.39×10^{-4}	1.02×10^{-5}	1.20×10^{-2}	1.66×10^5
(q)	1.3×10^{-2}	2.61×10^{-4}	1.11×10^{-5}	1.30×10^{-2}	1.49×10^5

5.2. Optimal configuration subjected to a minimum output voltage constraint

Herein, the efficacy of the introduced constraint with respect to output voltage is critically examined. Consistently across all scenarios, the substrate-dependent constraint was enforced utilizing the fictitious physical function p . Moreover, the material domain was characterized by dual-level set functions, ϕ_{pe} and ϕ_{sb} , with the parameter τ_z assigned a value of 1.0×10^{-2} . Table 3 enumerates the parameters for the minimum output voltage constraint under various conditions, alongside their respective objective functions F_k , F_ω , and output voltage V_E . The optimal configurations for each scenario are graphically represented in Figure 5.

As shown in Table 3, the output voltage V_E obtained under condition (j) exceeded the stipulated minimum voltage constraint. However, under the other conditions, the output voltages were aligned exactly with their respective constraints highlighted the effectiveness and precision of the minimum output voltage constraint. Furthermore, as the output voltage constraint values increased, there was a concomitant reduction in the volume of the piezoelectric material domain, represented by Ω_{pe} . As elucidated by Eq. (12), this reduction in the volume of the piezoelectric material domain results in a diminished capacitance, which, in turn, amplifies the production voltage. Concomitantly, an increase in the \bar{V}_{minV} value invariably leads to a corresponding increase in both objective functions F_k and F_ω . It is cogent to infer that imposing a minimum output voltage constraint invariably curtails the potential for optimizing the objective functions F_k and F_ω .

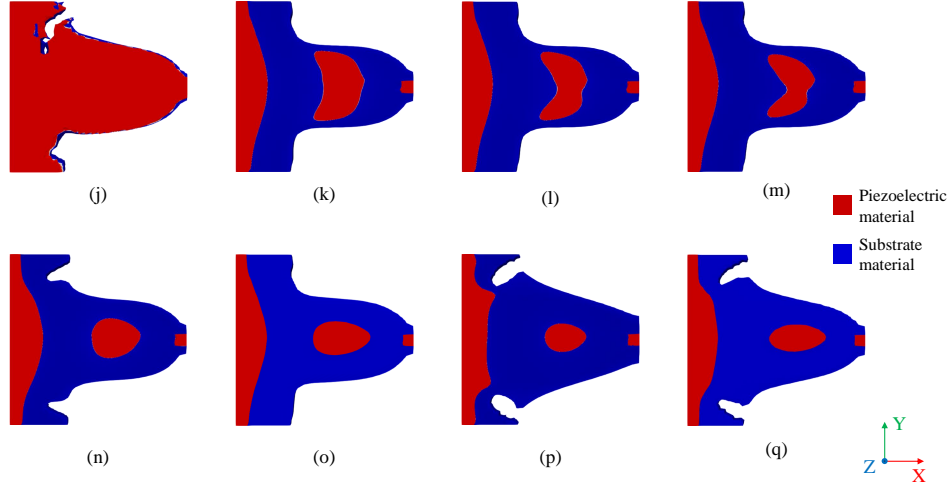


Figure 5: Optimal configuration of the unimorph cantilevered energy harvester for conditions (j)–(q), as detailed in Table 3. The red region denotes the piezoelectric material domain Ω_{pe} , and the blue region represents the substrate material domain Ω_{sb} .

As shown in Figure 5, under conditions (k)–(q) with an active minimum output voltage constraint, the piezoelectric material domain was predominantly located near the fixed boundary and at the midpoint of the beam. Proximate to the fixed boundary of the beam, the aggregation of the piezoelectric material domain can be attributed to the stress concentration observed in the first-order eigenmode. The region encompassing the piezoelectric material domain located around the center of the beam was aligned with the zone of maximal displacement in the second-order eigenmodes.

6. Conclusion

In this study, we proposed a method for designing piezoelectric energy harvesters to improve their manufacturability. The proposed method derives both the substrate and piezoelectric designs that maximize the electromechanical coupling coefficient. This method allows the eigenfrequency of the device and minimum output voltage to be set to the desired values. Furthermore, the proposed method yields a design that can be manufactured using a microfabrication process. The results of this study are summarized

as follows:

1. A topology optimization method was formulated to achieve the desired values for the eigenfrequency and minimum output voltage while concurrently maximizing the electromechanical coupling coefficient. An optimization algorithm was constructed for the numerical analysis.
2. Cross-sectional shape constraints and substrate-dependent constraints were formulated to improve manufacturability with microfabrication.
3. Several numerical examples were provided to demonstrate the utility and validity of the proposed method. The proposed method can provide solutions that satisfy the cross-sectional shape, substrate-depend, and minimum output voltage constraints.

6.1. Limitations and future work

Despite the promising results, this study has some limitations. As the constraints became more stringent, the value of the objective function deteriorated. This indicates that the proposed method may struggle to provide solutions with significant electrical-mechanical coupling coefficients under highly restrictive conditions.

In future work, we aim to actually manufacture devices based on the designs obtained through the proposed method. This will allow us to validate the practicality of the solutions obtained and further demonstrate the utility of the proposed method.

6.2. Final remarks

The proposed method for designing piezoelectric energy harvesters has shown significant potential for improving their manufacturability. We believe that this research contributes to the field of energy harvesting and opens up new possibilities for the design of efficient and manufacturable energy harvesters.

Appendix A. Computation of the output voltage using the modal superposition method

In this study, output voltage was computed using the modal superposition method. In Appendix A.1, we explain the method used to solve the eigenvalue problem using the finite element method(FEM). In Appendix A.2, we explain the method used to yield the output voltage using the modal superposition method based on the results obtained in Appendix A.1.

Appendix A.1. Eigenvalue and eigenvector determination

In this subsection, we elucidate an approach to solve the eigenvalue problem for piezoelectric materials using the FEM. Under open-circuit conditions, the relationships can be expressed in the form of finite element equations, as described below.

$$(\mathbf{K} + j\omega\mathbf{R} - \omega_{oc}^2\mathbf{M})\mathbf{u} + \mathbf{P}\varphi = 0, \quad (\text{A.1})$$

$$\mathbf{P}^T\mathbf{u} - \mathbf{G}\varphi = 0, \quad (\text{A.2})$$

wherein j denotes the imaginary unit; \mathbf{u} and φ correspond to the displacement and electric potential under open-circuit conditions, respectively; and \mathbf{P} and \mathbf{G} denote the piezoelectric and dielectric matrices, respectively. Notably, \mathbf{R} signifies the damping coefficient matrix inherent to the system. In the absence of an external charge, denoted by \mathbf{q} , and an external force, symbolized by \mathbf{f} , the potential φ can be eliminated. This leads to:

$$\mathbf{P}^T\mathbf{u} = \mathbf{G}\varphi, \quad (\text{A.3})$$

$$\varphi = \mathbf{G}^{-1}\mathbf{P}^T\mathbf{u},$$

$$(\mathbf{K} + j\omega\mathbf{R} - \omega^2\mathbf{M} + \mathbf{P}\mathbf{G}^{-1}\mathbf{P}^T)\mathbf{u} = 0. \quad (\text{A.4})$$

Consequently, the eigenvalue equation pertinent to the open-circuit conditions can be expressed as follows:

$$\mathbf{M}^{-1}(\mathbf{K} + \mathbf{P}\mathbf{G}^{-1}\mathbf{P}^T)\mathbf{u}_{oc} = \omega_{oc}^2\mathbf{u}_{oc}, \quad (\text{A.5})$$

where \mathbf{u}_{oc} represents the eigenvector associated with the eigenvalue ω_{oc} .

Conversely, for a short-circuited electrode, the potential difference between the electrodes is zero. By postulating that both the external charge \mathbf{q} and the external force \mathbf{f} are zero, analogous to the open-circuit condition, and by grounding the electrode to establish a zero potential, Eq. (6) yields the following equation:

$$(\mathbf{K} + j\omega\mathbf{R} - \omega^2\mathbf{M})\mathbf{u} = 0. \quad (\text{A.6})$$

The eigenvalue equation for the short-circuit condition is given as follows:

$$\mathbf{M}^{-1}\mathbf{K}\mathbf{u}_{sc} = \omega_{sc}^2\mathbf{u}_{sc}, \quad (\text{A.7})$$

where \mathbf{u}_{sc} represents the eigenvector corresponding to the eigenvalue ω_{sc} .

Appendix A.2. Evaluation of displacement and output voltage using the modal superposition method

Because the eigenvectors were normalized, it was necessary to consider the magnitude of displacement under forced vibration conditions to evaluate the output voltage. To achieve this, we utilized the modal superposition method to determine the displacement. First, the equation of motion is expressed as,

$$\mathbf{M}\ddot{\mathbf{u}} + \mathbf{C}\dot{\mathbf{u}} + \mathbf{K}\mathbf{u} = \mathbf{f}. \quad (\text{A.8})$$

For undamped free vibrations, we determined the eigenfrequency ω_{ocr} and the eigenvector \mathbf{u}_{oci} . Using the modal transformation matrix Φ , we performed a coordinate transformation such that $\mathbf{u} = \Phi\mathbf{q}$. The modal transformation matrix Φ is given by

$$\Phi = [\mathbf{u}_{oc1}, \mathbf{u}_{oc2}, \mathbf{u}_{oc3}, \dots, \mathbf{u}_{ocn}]. \quad (\text{A.9})$$

Multiplying Eq. (A.8) on the left with Φ^T , we obtain:

$$\Phi^T \mathbf{M} \Phi \ddot{\mathbf{q}} + \Phi^T \mathbf{C} \Phi \dot{\mathbf{q}} + \Phi^T \mathbf{K} \Phi \mathbf{q} = \Phi^T \mathbf{f}. \quad (\text{A.10})$$

Through normalization, we transform each coefficient term as,

$$\Phi^T \mathbf{M} \Phi = \mathbf{I}, \quad (\text{A.11})$$

$$\Phi^T \mathbf{C} \Phi = \mathbf{D} = \begin{bmatrix} 2\zeta_1\omega_1 & 0 & \dots & 0 \\ 0 & 2\zeta_2\omega_2 & \dots & 0 \\ \vdots & \vdots & \ddots & \vdots \\ 0 & 0 & \dots & 2\zeta_n\omega_n \end{bmatrix}, \quad (\text{A.12})$$

$$\Phi^T \mathbf{K} \Phi = \begin{bmatrix} \omega_1^2 & 0 & \dots & 0 \\ 0 & \omega_2^2 & \dots & 0 \\ \vdots & \vdots & \ddots & \vdots \\ 0 & 0 & \dots & \omega_n^2 \end{bmatrix}, \quad (\text{A.13})$$

$$\Phi^T \mathbf{f} = \begin{bmatrix} F_1(t) & 0 & \dots & 0 \\ 0 & F_2(t) & \dots & 0 \\ \vdots & \vdots & \ddots & \vdots \\ 0 & 0 & \dots & F_n(t) \end{bmatrix}. \quad (\text{A.14})$$

Assuming that the damping is small and the off-diagonal terms of the damping matrix are negligible compared with the diagonal terms, the transformation allowed us to express the motion Eq. (A.8) as n independent equations for each eigenmode as,

$$\ddot{q}_i(t) + 2\zeta_i\omega_i\dot{q}_i + \omega_i^2q_i(t) = F_i(t) \quad (i = 1, 2, \dots, n), \quad (\text{A.15})$$

$$q_i(t) = \frac{F_i(t)}{\omega_i \sqrt{(1 - (\bar{\omega}_i/\omega_i)^2)^2 + 4\zeta_i^2(\bar{\omega}_i/\omega_i)^2}}. \quad (\text{A.16})$$

From the above , displacement is yielded as follows:

$$\mathbf{u}(t) = \sum_{i=1}^n q_i(t) \mathbf{u}_{oci}. \quad (\text{A.17})$$

Incorporating this \mathbf{u} into Eq. (A.3) yields the potential φ . Notably, $\zeta_i = 0.01$ for $i = 1, 2, \dots, n$. Finally, incorporating φ into Eq. (10) yields the output voltage.

Appendix B. Sensitivity analysis

In this section, we provide a detailed description of the sensitivity analysis using mathematical formulations.

At the stationary point of the Lagrangian, the following optimality con-

ditions hold:

$$\left\{ \begin{array}{l} \left\langle \frac{\partial L_{pe}}{\partial \hat{\mathbf{u}}_{oc}}, \delta \mathbf{u}_{oc} \right\rangle \Big|_{opt} = \left\langle \frac{\partial (F_{pe} + a_{oc} + b_{oc})}{\partial \hat{\mathbf{u}}_{oc}}, \delta \mathbf{u}_{oc} \right\rangle \Big|_{opt} = 0, \quad (\text{B.1}) \\ \left\langle \frac{\partial L_{pe}}{\partial \mathbf{v}_{ocpe}}, \delta \mathbf{v}_{ocpe} \right\rangle \Big|_{opt} = \left\langle \frac{\partial (F_{pe} + a_{oc})}{\partial \mathbf{v}_{ocpe}}, \delta \mathbf{v}_{ocpe} \right\rangle \Big|_{opt} = 0, \quad (\text{B.2}) \\ \left\langle \frac{\partial L_{pe}}{\partial \hat{\varphi}_{oc}}, \delta \varphi_{oc} \right\rangle \Big|_{opt} = \left\langle \frac{\partial (F_{pe} + a_{oc} + b_{oc} + \lambda d_o)}{\partial \hat{\varphi}_{oc}}, \delta \varphi_{oc} \right\rangle \Big|_{opt} = 0, \quad (\text{B.3}) \\ \left\langle \frac{\partial L_{pe}}{\partial v_{\varphi_{ocpe}}}, \delta v_{\varphi_{ocpe}} \right\rangle \Big|_{opt} = \left\langle \frac{\partial (F_{pe} + b_{oc})}{\partial v_{\varphi_{ocpe}}}, \delta v_{\varphi_{ocpe}} \right\rangle \Big|_{opt} = 0, \quad (\text{B.4}) \\ \frac{\partial L_{pe}}{\partial \hat{\omega}_{oci}} \Big|_{opt} = \left\langle \frac{\partial (F_{pe} + a_{oc}(\omega_{oci}))}{\partial \hat{\omega}_{oci}}, \delta \omega_{oci} \right\rangle \Big|_{opt} = 0, \quad (\text{B.5}) \\ \left\langle \frac{\partial L_{pe}}{\partial \hat{\mathbf{u}}_{sc}}, \delta \mathbf{u}_{sc} \right\rangle \Big|_{opt} = \left\langle \frac{\partial (F_{pe} + a_{sc})}{\partial \hat{\mathbf{u}}_{sc}}, \delta \mathbf{u}_{sc} \right\rangle \Big|_{opt} = 0, \quad (\text{B.6}) \\ \left\langle \frac{\partial L_{pe}}{\partial \mathbf{v}_{scpe}}, \delta \mathbf{v}_{scpe} \right\rangle \Big|_{opt} = \left\langle \frac{\partial (F_{pe} + a_{sc})}{\partial \mathbf{v}_{scpe}}, \delta \mathbf{v}_{scpe} \right\rangle \Big|_{opt} = 0, \quad (\text{B.7}) \\ \frac{\partial L_{pe}}{\partial \hat{\omega}_{sci}} \Big|_{opt} = \left\langle \frac{\partial (F_{pe} + a_{sc}(\omega_{sci}))}{\partial \hat{\omega}_{sci}}, \delta \omega_{sci} \right\rangle \Big|_{opt} = 0, \quad (\text{B.8}) \end{array} \right.$$

$$\left\{ \begin{array}{l} \left\langle \frac{\partial L_{sb}}{\partial \hat{\mathbf{u}}_{oc}}, \delta \mathbf{u}_{oc} \right\rangle \Big|_{opt} = \left\langle \frac{\partial (F_{sb} + a_{oc} + b_{oc})}{\partial \hat{\mathbf{u}}_{oc}}, \delta \mathbf{u}_{oc} \right\rangle \Big|_{opt} = 0, \quad (\text{B.9}) \\ \left\langle \frac{\partial L_{sb}}{\partial \mathbf{v}_{ocsb}}, \delta \mathbf{v}_{ocsb} \right\rangle \Big|_{opt} = \left\langle \frac{\partial (F_{sb} + a_{oc})}{\partial \mathbf{v}_{ocsb}}, \delta \mathbf{v}_{ocsb} \right\rangle \Big|_{opt} = 0, \quad (\text{B.10}) \\ \left\langle \frac{\partial L_{sb}}{\partial \hat{\varphi}_{oc}}, \delta \varphi_{oc} \right\rangle \Big|_{opt} = \left\langle \frac{\partial (F_{sb} + a_{oc} + b_{oc} + \lambda d_o)}{\partial \hat{\varphi}_{oc}}, \delta \varphi_{oc} \right\rangle \Big|_{opt} = 0, \quad (\text{B.11}) \\ \left\langle \frac{\partial L_{sb}}{\partial v_{\varphi_{ocsb}}}, \delta v_{\varphi_{ocsb}} \right\rangle \Big|_{opt} = \left\langle \frac{\partial (F_{sb} + b_{oc})}{\partial v_{\varphi_{ocsb}}}, \delta v_{\varphi_{ocsb}} \right\rangle \Big|_{opt} = 0, \quad (\text{B.12}) \\ \frac{\partial L_{sb}}{\partial \hat{\omega}_{oci}} \Big|_{opt} = \left\langle \frac{\partial (F_{sb} + a_{oc}(\omega_{oci}))}{\partial \hat{\omega}_{oci}}, \delta \omega_{oci} \right\rangle \Big|_{opt} = 0, \quad (\text{B.13}) \\ \left\langle \frac{\partial L_{sb}}{\partial \hat{\mathbf{u}}_{sc}}, \delta \mathbf{u}_{sc} \right\rangle \Big|_{opt} = \left\langle \frac{\partial (F_{sb} + a_{sc})}{\partial \hat{\mathbf{u}}_{sc}}, \delta \mathbf{u}_{sc} \right\rangle \Big|_{opt} = 0, \quad (\text{B.14}) \\ \left\langle \frac{\partial L_{sb}}{\partial \mathbf{v}_{scsb}}, \delta \mathbf{v}_{scsb} \right\rangle \Big|_{opt} = \left\langle \frac{\partial (F_{sb} + a_{sc})}{\partial \mathbf{v}_{scsb}}, \delta \mathbf{v}_{scsb} \right\rangle \Big|_{opt} = 0, \quad (\text{B.15}) \\ \frac{\partial L_{sb}}{\partial \hat{\omega}_{sci}} \Big|_{opt} = \left\langle \frac{\partial (F_{sb} + a_{sc}(\omega_{sci}))}{\partial \hat{\omega}_{sci}}, \delta \omega_{sci} \right\rangle \Big|_{opt} = 0, \quad (\text{B.16}) \end{array} \right.$$

where the expressions within the brackets represent the directional derivatives of the functional. The optimality conditions, defined by Eqs. (B.1)–(B.16), revealed that the variables $\hat{\mathbf{u}}_{oc}$, $\hat{\mathbf{u}}_{sc}$, $\hat{\varphi}_{oc}$, $\hat{\omega}_{oc}$, and $\hat{\omega}_{sc}$ coincides with state the variables \mathbf{u}_{oc} , \mathbf{u}_{sc} , φ_{oc} , ω_{oc} , and ω_{sc} , respectively.

Eqs. (B.1), (B.3), and (B.5) can be used to derive \mathbf{v}_{ocpe} , \mathbf{v}_{ocsb} , \mathbf{v}_{scpe} , \mathbf{v}_{scsb} , $v_{\varphi_{ocpe}}$, and $v_{\varphi_{ocsb}}$ as follows:

$$\mathbf{v}_{ocpe} = c_{ocpe} \mathbf{u}_{oc}, \quad \mathbf{v}_{scpe} = c_{scpe} \mathbf{u}_{sc}, \quad v_{\varphi_{ocpe}} = c_{ocpe} \varphi_{oc}, \quad (\text{B.17})$$

$$c_{ocpe} = \frac{-\alpha_{pe} \omega_{sc}^2}{(\omega_{oc}^2 - \omega_{sc}^2)^2} + (1 - \alpha_{pe}) \sum_{i=1}^n \frac{(\omega_{oci} - \bar{\omega}_i)}{\omega_{oci} \bar{\omega}_i^2}, \quad (\text{B.18})$$

$$c_{scpe} = \frac{\alpha_{pe} \omega_{oc}^2}{(\omega_{oc}^2 - \omega_{sc}^2)^2}. \quad (\text{B.19})$$

$$\mathbf{v}_{ocsb} = c_{ocsb} \mathbf{u}_{oc}, \quad \mathbf{v}_{scsb} = c_{scsb} \mathbf{u}_{sc}, \quad v_{\varphi_{ocsb}} = c_{ocsb} \varphi_{oc}, \quad (\text{B.20})$$

$$c_{ocsb} = \frac{-\alpha_{sb} \omega_{sc}^2}{(\omega_{oc}^2 - \omega_{sc}^2)^2} + (1 - \alpha_{sb}) \sum_{i=1}^n \frac{(\omega_{oci} - \bar{\omega}_i)}{\omega_{oci} \bar{\omega}_i^2}, \quad (\text{B.21})$$

$$c_{scsb} = \frac{\alpha_{sb} \omega_{oc}^2}{(\omega_{oc}^2 - \omega_{sc}^2)^2}. \quad (\text{B.22})$$

From the above equations, the sensitivities for updating ϕ_{pe} and ϕ_{sb} can be obtained as follows:

$$\begin{aligned} F'_{pe} &= \frac{\partial L_{pe}}{\partial \phi_{pe}} = c_{ocpe} \left\{ \frac{\partial a_{oc}(\phi_{pe}, \phi_{sb}, \omega_{oc}, \mathbf{u}_{oc}, \mathbf{u}_{oc}, \varphi_{oc})}{\partial \phi_{pe}} + \frac{\partial b_{oc}(\phi_{pe}, \mathbf{u}_{oc}, \varphi_{oc}, \varphi_{oc})}{\partial \phi_{pe}} \right\} \\ &\quad + c_{scpe} \left\{ \frac{\partial a_{sc}(\phi_{pe}, \phi_{sb}, \omega_{sc}, \mathbf{u}_{sc}, \mathbf{u}_{sc})}{\partial \phi_{pe}} \right\} + \lambda, \\ &= c_{ocpe} \{ a_{oc}(1, \phi_{sb}, \omega_{oc}, \mathbf{u}_{oc}, \mathbf{u}_{oc}, \varphi_{oc}) + b_{oc}(1, \mathbf{u}_{oc}, \varphi_{oc}, \varphi_{oc}) \} \\ &\quad + c_{scpe} a_{sc}(1, \phi_{sb}, \omega_{sc}, \mathbf{u}_{sc}, \mathbf{u}_{sc}) + \lambda, \end{aligned} \quad (\text{B.23})$$

$$\begin{aligned} F'_{sb} &= \frac{\partial L_{sb}}{\partial \phi_{sb}} = c_{ocsb} \left\{ \frac{\partial a_{oc}(\phi_{pe}, \phi_{sb}, \omega_{oc}, \mathbf{u}_{oc}, \mathbf{u}_{oc}, \varphi_{oc})}{\partial \phi_{sb}} + \frac{\partial b_{oc}(\phi_{pe}, \mathbf{u}_{oc}, \varphi_{oc}, \varphi_{oc})}{\partial \phi_{sb}} \right\} \\ &\quad + c_{scsb} \left\{ \frac{\partial a_{sc}(\phi_{pe}, \phi_{sb}, \omega_{sc}, \mathbf{u}_{sc}, \mathbf{u}_{sc})}{\partial \phi_{sb}} \right\}, \\ &= c_{ocsb} \{ a_{oc}(\phi_{pe}, 1, \omega_{oc}, \mathbf{u}_{oc}, \mathbf{u}_{oc}, \varphi_{oc}) \} \\ &\quad + c_{scsb} \{ a_{sc}(\phi_{pe}, 1, \omega_{sc}, \mathbf{u}_{sc}, \mathbf{u}_{sc}) \}. \end{aligned} \quad (\text{B.24})$$

References

- [1] Y. B. Jeon, R. Sood, J.-h. Jeong, S.-G. Kim, Mems power generator with transverse mode thin film pzt, *Sensors and Actuators A: Physical* 122 (2005) 16–22.
- [2] S. Roundy, P. K. Wright, J. Rabaey, A study of low level vibrations as a power source for wireless sensor nodes, *Computer communications* 26 (2003) 1131–1144.
- [3] S. M. Yun, C. Kim, The vibrating piezoelectric cantilevered generator under vortex shedding excitation and voltage tests, *International Journal of Precision Engineering and Manufacturing* 17 (2016) 1615–1622.

- [4] A. Erturk, D. J. Inman, Piezoelectric energy harvesting, John Wiley & Sons, 2011.
- [5] K. A. Cook-Chennault, N. Thambi, A. M. Sastry, Powering mems portable devices - a review of non-regenerative and regenerative power supply systems with special emphasis on piezoelectric energy harvesting systems, *Smart materials and structures* 17 (2008) 043001.
- [6] S. P. Beeby, M. J. Tudor, N. White, Energy harvesting vibration sources for microsystems applications, *Measurement science and technology* 17 (2006) R175.
- [7] S. Saxena, R. Sharma, B. Pant, Design and development of MEMS based guided beam type piezoelectric energy harvester, Springer, 2021.
- [8] T. Yoshimura, S. Murakami, K. Wakazono, K. Kariya, N. Fujimura, Piezoelectric vibrational energy harvester using lead-free ferroelectric bifeo3 films, *Applied Physics Express* 6 (2013) 051501.
- [9] S. Murakami, T. Yoshimura, K. Satoh, K. Wakazono, K. Kariya, N. Fujimura, Development of piezoelectric mems vibration energy harvester using (100) oriented bifeo3 ferroelectric film, *Journal of Physics: Conference Series* 476 (2013) 012007.
- [10] P. Glynn-Jones, S. P. Beeby, N. M. White, Towards a piezoelectric vibration-powered microgenerator, *IEE Proceedings-Science, measurement and technology* 148 (2001) 68–72.
- [11] M. P. Bendsøe, N. Kikuchi, Generating optimal topologies in structural design using a homogenization method, *Computer Methods in Applied Mechanics and Engineering* 71 (1988) 197–224.
- [12] E. C. N. Silva, J. S. Ono Fonseca, N. Kikuchi, Optimal design of periodic piezocomposites, *Computer Methods in Applied Mechanics and Engineering* 159 (1998) 49–77.
- [13] B. Zheng, C. J. Chang, H. C. Gea, Topology optimization of energy harvesting devices using piezoelectric materials, *Structural and Multidisciplinary Optimization* 38 (2009) 17–23.

- [14] C. J. Rupp, A. Evgrafov, K. Maute, M. L. Dunn, Design of piezoelectric energy harvesting systems: a topology optimization approach based on multilayer plates and shells, *Journal of Intelligent Material Systems and Structures* 20 (2009) 1923–1939.
- [15] M. Kögl, E. C. N. Silva, Topology optimization of smart structures: design of piezoelectric plate and shell actuators, *Smart materials and Structures* 14 (2005) 387.
- [16] Z. Kang, L. Tong, Integrated optimization of material layout and control voltage for piezoelectric laminated plates, *Journal of Intelligent Material Systems and Structures* 19 (2008) 889–904.
- [17] X. Zhang, Z. Kang, Dynamic topology optimization of piezoelectric structures with active control for reducing transient response, *Computer Methods in Applied Mechanics and Engineering* 281 (2014) 200–219.
- [18] S. Chen, S. Gonella, W. Chen, W. K. Liu, A level set approach for optimal design of smart energy harvesters, *Computer Methods in Applied Mechanics and Engineering* 199 (2010) 2532–2543.
- [19] Z. Luo, L. Tong, J. Luo, P. Wei, M. Y. Wang, Design of piezoelectric actuators using a multiphase level set method of piecewise constants, *Journal of Computational Physics* 228 (2009) 2643–2659.
- [20] M. He, M. He, X. Zhang, L. Xia, Topology optimization of piezoelectric energy harvesters for enhanced open-circuit voltage subjected to harmonic excitations, *Materials* 15 (2022) 4423.
- [21] B. V. de Almeida, D. C. Cunha, R. Pavanetto, Topology optimization of bimorph piezoelectric energy harvesters considering variable electrode location, *Smart Materials and Structures* 28 (2019) 085030.
- [22] C. Kim, J. Lee, Topology optimum design of unimorph piezoelectric cantilevered mindlin plates as a vibrating electric harvester, *Journal of Mechanical Science and Technology* 28 (2014) 4131–4138.
- [23] G. H. Yoon, H. Choi, S. Hur, Multiphysics topology optimization for piezoelectric acoustic focuser, *Computer Methods in Applied Mechanics and Engineering* 332 (2018) 600–623.

- [24] R. A. Salas, F. J. Ramírez-Gil, W. Montealegre-Rubio, E. C. N. Silva, J. Reddy, Optimized dynamic design of laminated piezocomposite multi-entry actuators considering fiber orientation, *Computer Methods in Applied Mechanics and Engineering* 335 (2018) 223–254.
- [25] R. A. Salas, A. L. F. da Silva, E. C. N. Silva, HYIMFO: Hybrid method for optimizing fiber orientation angles in laminated piezocomposite actuators, *Computer Methods in Applied Mechanics and Engineering* 385 (2021) 114010.
- [26] Y. Sato, T. Yamada, K. Izui, S. Nishiwaki, Manufacturability evaluation for molded parts using fictitious physical models, and its application in topology optimization, *The International Journal of Advanced Manufacturing Technology* 92 (2017) 1391–1409.
- [27] T. Yamada, Y. Noguchi, Topology optimization with a closed cavity exclusion constraint for additive manufacturing based on the fictitious physical model approach, *Additive Manufacturing* 52 (2022) 102630.
- [28] M. Tajima, T. Yamada, Topology optimization with geometric constraints for additive manufacturing based on coupled fictitious physical model, *Computer Methods in Applied Mechanics and Engineering* 417 (2023) 116415.
- [29] T. Yamada, K. Izui, S. Nishiwaki, A. Takezawa, A topology optimization method based on the level set method incorporating a fictitious interface energy, *Computer Methods in Applied Mechanics and Engineering* 199 (2010) 2876–2891.
- [30] M. Noda, Y. Noguchi, T. Yamada, Extended level set method: A multiphase representation with perfect symmetric property, and its application to multi-material topology optimization, *Computer Methods in Applied Mechanics and Engineering* 393 (2022) 114742.
- [31] M. Aramaki, T. Yoshimura, S. Murakami, K. Satoh, N. Fujimura, Demonstration of high-performance piezoelectric mems vibration energy harvester using bifeo3 film with improved electromechanical coupling factor, *Sensors and Actuators A: Physical* 291 (2019) 167–173.

- [32] N. W. Hagood, A. von Flotow, Damping of structural vibrations with piezoelectric materials and passive electrical networks, *Journal of sound and vibration* 146 (1991) 243–268.
- [33] T. Yamada, T. Matsumoto, S. Nishiwaki, Generating structural configurations having a number of specified eigenfrequencies using a level set-based topology optimization method, *Civil-Comp Proceedings* 99 (2012) 1–11.
- [34] G. Allaire, *Shape optimization by the homogenization method*, volume 146, Springer Science & Business Media, 2001.
- [35] M. Zhou, Y. Liu, Z. Lin, Topology optimization of thermal conductive support structures for laser additive manufacturing, *Computer Methods in Applied Mechanics and Engineering* 353 (2019) 24–43.
- [36] T. Yamada, K. Izui, S. Nishiwaki, A level set-based topology optimization method for maximizing thermal diffusivity in problems including design-dependent effects, *Journal of Mechanical Design* 133 (2011). 031011.
- [37] G. Jing, H. Isakari, T. Matsumoto, T. Yamada, T. Takahashi, Level set-based topology optimization for 2D heat conduction problems using BEM with objective function defined on design-dependent boundary with heat transfer boundary condition, *Engineering Analysis with Boundary Elements* 61 (2015) 61–70.
- [38] C. Wu, J. Fang, Q. Li, Multi-material topology optimization for thermal buckling criteria, *Computer Methods in Applied Mechanics and Engineering* 346 (2019) 1136–1155.
- [39] T. Miki, T. Yamada, Topology optimization considering the distortion in additive manufacturing, *Finite Elements in Analysis and Design* 193 (2021) 103558.
- [40] F. Feppon, G. Allaire, C. Dapogny, P. Jolivet, Topology optimization of thermal fluid-structure systems using body-fitted meshes and parallel computing, *Journal of Computational Physics* 417 (2020) 109574.

- [41] K. Guan, K. Matsushima, Y. Noguchi, T. Yamada, Topology optimization for rarefied gas flow problems using density method and adjoint IP-DSMC, *Journal of Computational Physics* 474 (2023) 111788.
- [42] J. S. Choi, J. Yoo, Simultaneous structural topology optimization of electromagnetic sources and ferromagnetic materials, *Computer Methods in Applied Mechanics and Engineering* 198 (2009) 2111–2121.
- [43] T. Yamada, H. Watanabe, G. Fujii, T. Matsumoto, Topology optimization for a dielectric optical cloak based on an exact level set approach, *IEEE Transactions on Magnetics* 49 (2013) 2073–2076.
- [44] E. Wadbro, M. Berggren, Topology optimization of an acoustic horn, *Computer Methods in Applied Mechanics and Engineering* 196 (2006) 420–436.
- [45] O. Sigmund, J. S. Jensen, Systematic design of phononic band-gap materials and structures by topology optimization, *Philosophical Transactions of the Royal Society of London. Series A: Mathematical, Physical and Engineering Sciences* 361 (2003) 1001–1019.
- [46] Y. Noguchi, T. Yamada, Topology optimization for acoustic structures considering viscous and thermal boundary layers using a sequential linearized navier-stokes model, *Computer Methods in Applied Mechanics and Engineering* 394 (2022) 114863.
- [47] Y. Noguchi, T. Yamada, Topology optimization of acoustic metasurfaces by using a two-scale homogenization method, *Applied Mathematical Modelling* 98 (2021) 465–497.
- [48] F. Laermer, Method of anisotropically etching silicon, *United States Patent* 5,501,893 (1996).
- [49] F. Hecht, New development in freefem++, *J. Numer. Math.* 20 (2012) 251–265. URL: <https://freefem.org/>.
- [50] G. Allaire, F. Jouve, A. M. Toader, Structural optimization using sensitivity analysis and a level-set method, *Journal of computational physics* 194 (2004) 363–393.